

# BMapOpt: Optimization of Brain Tissue Probability Maps using a Differentiable MRI Simulator

Utkarsh Gupta<sup>1</sup>, Emmanouil Nikolakis<sup>2</sup>, Moritz Zaiss<sup>3,4</sup>, and Razvan Marinescu<sup>1</sup>

<sup>1</sup> University of California, Santa Cruz, Computer Science and Engineering Department

<sup>2</sup> University of California, Santa Cruz, Electrical and Computer Engineering Department

<sup>3</sup> Department of Neuroradiology, Universitätsklinik Erlangen, Erlangen, Germany

<sup>4</sup> Department of Artificial Intelligence in Biomedical Engineering,  
Friedrich-Alexander-Universität Erlangen Nürnberg, Erlangen, Germany

**Abstract.** Reconstructing digital brain phantoms in the form of multi-channeled brain tissue probability maps for individual subjects is essential for capturing brain anatomical variability, understanding neurological diseases, as well as for testing image processing methods. We demonstrate the first framework that optimizes brain tissue probability maps (Gray Matter - GM, White Matter - WM, and Cerebrospinal fluid - CSF) with the help of a Physics-based differentiable MRI simulator that models the magnetization signal at each voxel in the image. Given an observed  $T_1/T_2$ -weighted MRI scan, the corresponding clinical MRI sequence, and the MRI differentiable simulator, we optimize the simulator's input probability maps by back-propagating the L2 loss between the simulator's output and the  $T_1/T_2$ -weighted scan. This approach has the significant advantage of not relying on any training data, and instead uses the strong inductive bias of the MRI simulator. We tested the model on 20 scans from the BrainWeb database and demonstrate a highly accurate reconstruction of GM, WM, and CSF.

**Keywords:** Tissue probability maps · Differentiable MRI simulator · Input optimization.

## 1 Introduction

Quantitative  $T_1$  ( $qT_1$ ) and  $T_2$  ( $qT_2$ ) MRI plays a pivotal role in understanding various neurological conditions, including multiple sclerosis [10], brain tumors [6], and neurodegenerative diseases such as Alzheimer's [16], by providing valuable insights into tissue characteristics and pathological changes. However, even more information than  $T_1/T_2$  MRI can be obtained by reconstructing digital brain phantoms, which can be represented as brain tissue probability maps. The BrainWeb phantoms [8,2] are among the most popular such phantoms, where at each voxel, they store a vector of probabilities for 11 tissues, which include CSF, GM, WM, fat, muscles, skull, blood vessels, dura matter, and bone marrow. These phantoms offer significant advantages such as more precise anatomical detail than  $qT_1/qT_2$  maps, customizable tissue properties, and the ability to simulate realistic imaging scenarios. Despite their utility, no method exists that can automatically infer digital phantoms, which are the input to simulation-based MR imaging. Additionally, the problem is particularly challenging due to its ill-posedness

at two different levels: 1) there can be multiple digital phantoms corresponding to a set of  $qT_1/qT_2/PD$  maps, and 2) there can be multiple  $qT_1/qT_2/PD$  maps corresponding to a single  $T_1$ - or  $T_2$ -weighted image.

MRI imaging simulators [5,22,19,20,15,26,4,13,21,3,25,24,7] offer a solution for inferring digital brain phantoms. These simulators generally take  $qT_1$ ,  $qT_2$ , and PD maps as input alongside an MRI sequence specifying the echo time (TE), repetition time (TR), flip angles, gradients, etc. By utilizing a forward model, they can be used to generate k-space measurements and subsequently reconstruct  $T_1/T_2$ -weighted scans. However, optimizing the phantom is only computationally feasible if the simulator is implemented in a differentiable manner. This is because, when optimizing in this high-dimensional space of MRI images, derivative-free methods such as Markov Chain Monte Carlo, Coordinate Descent, or Nelder-Mead would require too many forward passes to converge to the correct solution and would easily get stuck in local minima.

A recent innovation in the MRI simulators domain is the building of MR-zero [17], a differentiable MRI simulator implementing the Phase Distribution Graph [9]. This represents a paradigm shift in medical imaging simulation and optimization. By leveraging these simulators, it becomes feasible to fine-tune the parameters of clinical sequences, leading to enhanced image quality, reduced artifacts, and improved diagnostic accuracy. Moreover, the inherent physics-based inductive biases embedded within differentiable simulators facilitate the optimization of quantitative  $T_1$ ,  $T_2$ , and PD maps, opening up the possibility of optimizing more intricate aspects like brain tissue probability maps.

In this paper, we introduce a novel framework leveraging the capabilities of MR-zero to estimate digital brain phantoms in the form of tissue probability maps (Fig. 2) encompassing Cerebrospinal Fluid (CSF), Gray Matter (GM), and White Matter (WM). Moreover, our framework can estimate *patient-specific* tissue probability maps given the observed  $T_1/T_2$ -weighted scan, and does not require one-to-one mapping for digital brain phantom and observed MRI scans. Through comprehensive experimentation and validation on the 20 subjects of the BrainWeb dataset, we demonstrate our proposed framework's efficacy and potential impact in advancing state-of-the-art in MRI imaging and Neuroimaging research. Our contributions are:

- We demonstrate the possibility of optimizing brain tissue probability maps using the differentiable MRI simulator that conducts forward inference to generate a  $T_1/T_2$ -weighted image and by backpropagating a loss function to the brain tissue probability maps. This approach is versatile, applicable to various MRI sequences, and does not require any training dataset or additional learnable parameters.
- We overcome the ill-posedness of brain probability maps inference through the use of multiple  $T_1/T_2$  contrasts.
- We validated our approach on 20 subjects of the BrainWeb dataset and popular variants of the Fast Low Angle Shot (FLASH) sequence, providing empirical evidence of its effectiveness and demonstrating its applicability in real-world medical imaging settings.

## 2 Methodology

### 2.1 Extended Phase Graph

Extended Phase Graphs (EPG) [23] are a powerful way to simulate the magnetization response of a broad variety of MR sequences. A key aspect of EPG involves the manipulation of magnetization vectors through changes in a Fourier basis. Initially, the longitudinal  $M_z(z)$  and transverse  $M_{xy}$  and  $M_{xy}^*$  magnetization components are projected on a Fourier basis to obtain the Fourier components  $F_n^+$ ,  $F_n^-$ , and  $Z_n$ :

$$F_n^+ = \int_0^1 M_{xy}(z) e^{-2\pi\iota n z} dz \quad F_n^- = \int_0^1 M_{xy}^*(z) e^{-2\pi\iota n z} dz$$

$$Z_n = \int_0^1 M_z(z) e^{-2\pi\iota n z} dz \quad Q = \begin{bmatrix} F_0^+ & F_1^+ & F_2^+ & \dots & F_N^+ \\ F_0^{+*} & F_1^- & F_2^- & \dots & F_N^- \\ Z_0 & Z_1 & Z_2 & \dots & Z_N \end{bmatrix}$$

The F states are then combined across  $n$  harmonics to form the EPG basis  $Q$  (shown above), which describes the magnetization state in one isochromat. Using the above EPG formalization, we can model the spin precession as a matrix operation:

$$\begin{bmatrix} F_n^+ \\ F_n^- \\ Z_n \end{bmatrix}' = \begin{bmatrix} e^{\iota\theta} & 0 & 0 \\ 0 & e^{-\iota\theta} & 0 \\ 0 & 0 & 1 \end{bmatrix} \begin{bmatrix} F_n^+ \\ F_n^- \\ Z_n \end{bmatrix} \quad (1)$$

where  $\theta$  is the accumulated phase. Similarly, an RF pulse that flips the magnetization longitudinally by  $\alpha$  and transversally by  $\phi$  as:

$$\begin{bmatrix} F_n^+ \\ F_n^- \\ Z_n \end{bmatrix}' = \begin{bmatrix} \cos^2(\alpha/2) & e^{2\iota\phi}\sin^2(\alpha/2) & -ie^{\iota\phi}\sin(\alpha) \\ e^{-2\iota\phi}\sin^2(\alpha/2) & \cos^2(\alpha/2) & ie^{-\iota\phi}\sin(\alpha) \\ -\frac{\iota}{2e^{-\iota\phi}\sin(\alpha)} & \frac{\iota}{2e^{\iota\phi}\sin(\alpha)} & \cos(\alpha) \end{bmatrix} \begin{bmatrix} F_n^+ \\ F_n^- \\ Z_n \end{bmatrix} \quad (2)$$

Similarly the above linear operations can also be used for modeling gradients and relaxation. Therefore, an MRI clinical sequence of events (RF pulses, gradients, precession, relaxation, etc.) is simulated as a multiplication of  $Q$  (representing the voxel's state) through several matrices corresponding to precession, RF rotations, relaxation operators, and gradients. Until recently, EPG could only describe echo amplitudes, which was extended by Phase Distribution Graphs (PDG) [9] to describe full echo shapes, including gradient echoes that provide spatial encoding.

### 2.2 MRI Differentiable Simulator

MR-zero [17] is an MRI simulation tool that uses PDG to simulate the magnetization changes based on the MRI sequence events and input  $T_1$ ,  $T_2$ , and Proton Density (PD) maps. MR-zero can simulate arbitrary MRI sequences, including clinical MRI sequences, such as Spin-Echo [14], Gradient Recalled Echo [18], Rapid Acquisition with Relaxation Enhancement [12], and Fast Low Angle Shot [11], etc. As opposed

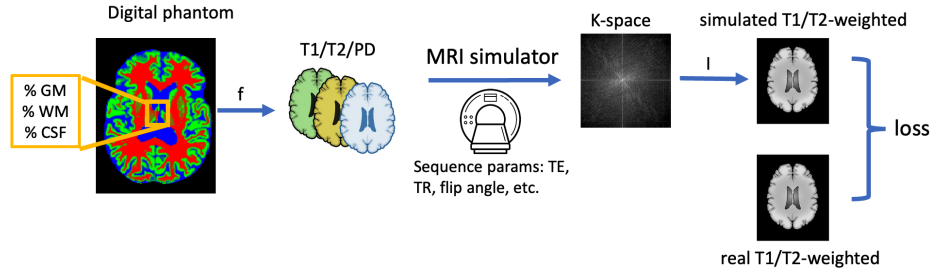


Fig. 1: Optimization pipeline

to previous simulators such as [5][22][19][20][15][26][4], MR-zero is implemented in PyTorch and is differentiable by design. This allows us to incorporate MR-zero as part of the forward inference pipeline through which backpropagation can be performed, allowing one to efficiently optimize the input  $T_1/T_2$ /PD maps or the MRI sequence given a  $T_1/T_2$ -weighted image.

The simulation process in MR-zero comprises two passes: The first pass swiftly simulates numerous states to provide an initial estimate of the signal. This step identifies crucial states contributing to the signal and discards irrelevant ones. Secondly, the main pass utilizes the precise signal equation, considering all voxels but minimizing the number of simulated states based on information gleaned from the pre-pass. Doing so generates a meaningful signal suitable for reconstructing  $T_1/T_2$ -weighted scans as output.

### 2.3 Probability Maps Optimization

Our framework optimizes brain tissue probability maps given one or more observed  $T_1/T_2$ -weighted MRI scans ( $G$ ) and the corresponding MRI clinical sequence ( $S$ ) used to generate each scan (Fig. 1). The optimization pipeline begins by transforming the brain tissue probability maps into  $T_1$  relaxation,  $T_2$  relaxation, Proton Density (PD) maps with the help of known relaxation time values for 1.5T scanner [1]. These maps serve as input for the MR-zero MRI differentiable simulator that produces K-space measurements as its output of the forward pass. By applying the Inverse Fourier Transform ( $I$ ), the simulated  $T_1/T_2$ -weighted scan ( $G'$ ) is reconstructed from K-space. Therefore, the end-to-end forward pass is given as follows:

$$G' = I(MRZero(f(GM, WM, CSF), S)) \quad (3)$$

where  $f$  is a fixed linear transformation function for probability maps. The pixel-wise L2 loss  $\|G - G'\|_2^2$  is calculated between the observed  $T_1/T_2$ -weighted scan  $G'$  and the ground truth scan  $G$  and backpropagated to the input probability maps.

### 3 Experiments

**Dataset** We utilized the BrainWeb dataset to showcase the optimization of brain tissue probability maps. This dataset comprises brain tissue probability maps from 20 subjects. We downscaled the 3D brain volumes and selected their middle slice, resulting in CSF, GM, and WM probability maps of 64x64 dimensions each.

**Ill-posed problem** The optimization of tissue probability maps presents a challenge due to the inherent ambiguity stemming from the ill-posed nature of the problem, wherein multiple potential solutions (tissue probabilities) exist for a single observed  $T_1/T_2$ -weighted scan. We experimented with a single observed contrast obtained from the  $T_1$  inversion recovery (Table 1) MRI clinical sequence to demonstrate the ill-posed nature of estimation. Furthermore, the sensitivity of tissue delineation is influenced by the specific MRI clinical sequence utilized. For instance, the Fluid Attenuated Inversion Recovery (FLAIR) sequence effectively diminishes the signal from CSF, resulting in a brighter appearance for GM in the captured image. To address the challenge posed by the ill-posed nature of the problem, we have augmented the optimization process by incorporating additional output contrasts obtained from capturing images at varying echo times and by including a diverse array of sequences such as  $T_2$ -weighted imaging,  $T_2^*$  imaging through echo time alterations, FLAIR, Double Inversion Recovery (DIR), and Diffusion Weighted Imaging (DWI) sequences.

**Setup** Our optimization process spans 501 epochs with a learning rate of 0.01. We perform the optimization of all probability maps (CSF, GM, and WM) concurrently, leveraging the output contrasts from up to six different MRI clinical sequences. Loss computation is conducted across 24 reconstructed image spaces, representing the output  $T_1/T_2$ -weighted scans (each with four contrasts per sequence). This is the baseline configuration settings for comparing the results. We performed leave-one-out cross-validation. Our approach doesn't introduce any additional learnable parameters beyond the probability maps themselves.

### 4 Results

**Ill-posed problem** As illustrated in Table 1 and in Fig. 2, the PSNRs and SSIMs  $(17.84 \pm 1.18, 0.58 \pm 0.07)$ ,  $(14.22 \pm 0.97, 0.57 \pm 0.08)$ ,  $(12.83 \pm 1.1, 0.38 \pm 0.07)$  for CSF, GM, and WM respectively for the  $T_1$ -inversion recovery single contrast sequence reveal notably poor performance. As we add more sequences, the PSNR and SSIM improves to  $(34.64 \pm 5.29, 0.98 \pm 0.02)$ ,  $(27.71 \pm 2.48, 0.97 \pm 0.02)$ , and  $(27.0 \pm 2.69, 0.93 \pm 0.03)$  for CSF, GM, and WM respectively up to the addition of FLAIR sequence. These numbers were contrary to our expectation that adding more sequences should always improve the metrics; adding the Diffusion Weighted Imaging sequence leads to an average drop of 0.7 in PSNR and 0.007 in SSIM scores for all three maps.

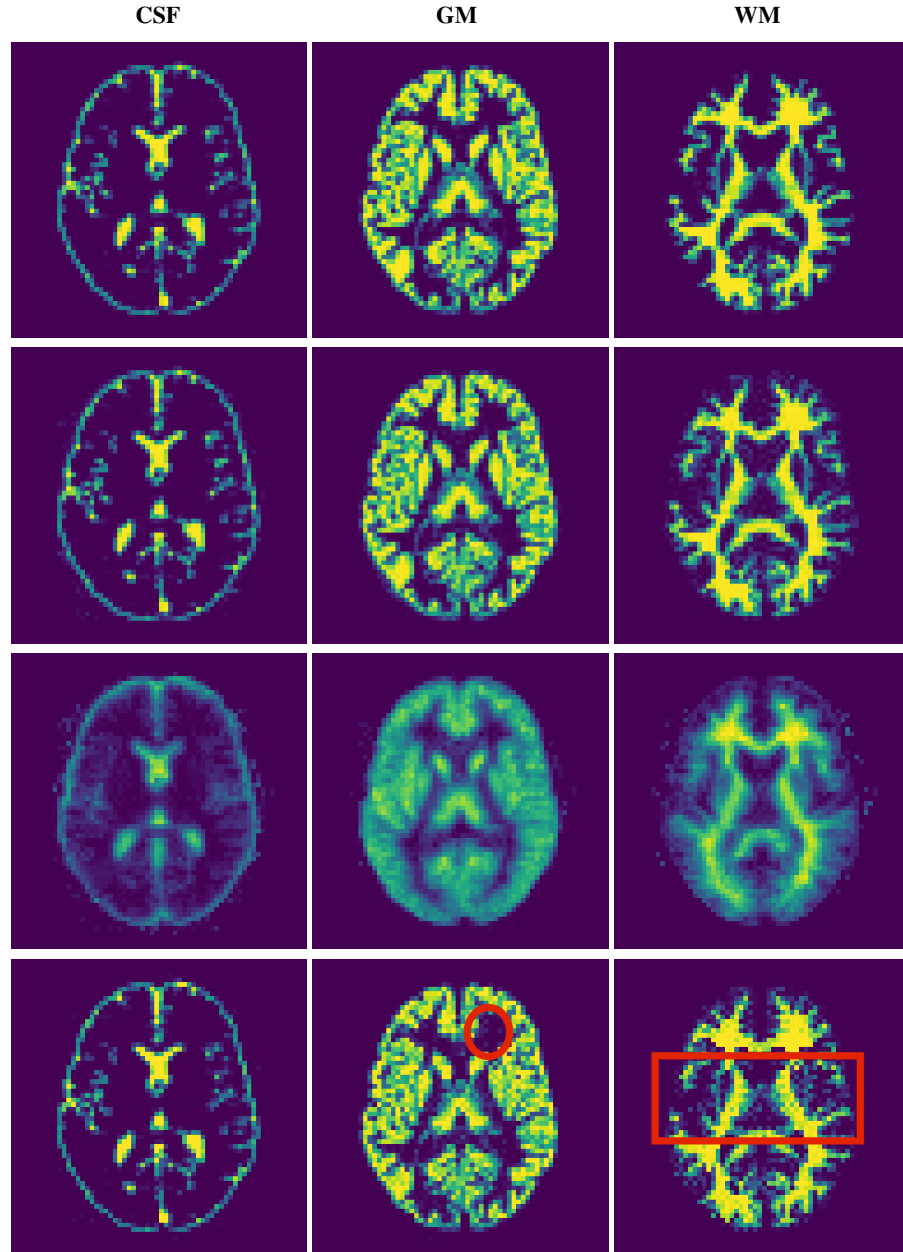


Fig. 2: From the left are CSF, GM, and WM. The first row shows the raw tissue probability maps for subject 42 in BrainWeb dataset. The second row shows the optimized probability maps using the baseline configuration. The third row shows the ill-posed optimization using the single contrast from the  $T_1$  inversion recovery sequence. The fourth row shows the checkerboard pattern enclosed in red marked region while optimizing 19 linear coefficients instead of probability maps directly.

Table 1: PSNR and SSIM comparisons for a combination of MRI clinical sequences. Except for the first row, all the experiments use 4 contrasts per sequence.  $\dagger$  represents the baseline configuration.

Contrasts	CSF		GM		WM	
	PSNR $\uparrow$	SSIM $\uparrow$	PSNR $\uparrow$	SSIM $\uparrow$	PSNR $\uparrow$	SSIM $\uparrow$
$T_1$ single contrast	17.84 $\pm$ 1.18	0.58 $\pm$ 0.07	14.22 $\pm$ 0.97	0.57 $\pm$ 0.08	12.83 $\pm$ 1.1	0.38 $\pm$ 0.07
$T_1$ four contrasts	27.57 $\pm$ 2.11	0.89 $\pm$ 0.03	16.16 $\pm$ 0.97	0.74 $\pm$ 0.05	18.15 $\pm$ 0.98	0.78 $\pm$ 0.04
$T_1 + T_2$	30.9 $\pm$ 3.93	0.97 $\pm$ 0.02	23.5 $\pm$ 1.98	0.93 $\pm$ 0.03	25.63 $\pm$ 2.43	0.93 $\pm$ 0.03
$T_1 + T_2 + T_2^*$	33.43 $\pm$ 4.72	0.97 $\pm$ 0.02	26.38 $\pm$ 2.35	0.96 $\pm$ 0.03	25.16 $\pm$ 2.34	0.91 $\pm$ 0.03
$T_1 + T_2 + T_2^* + \text{DIR}$	33.68 $\pm$ 4.51	0.97 $\pm$ 0.02	26.33 $\pm$ 2.38	0.96 $\pm$ 0.03	25.16 $\pm$ 2.45	0.91 $\pm$ 0.04
$T_1 + T_2 + T_2^* + \text{DIR} + \text{FLAIR}$	<b>34.64<math>\pm</math>5.29</b>	<b>0.98<math>\pm</math>0.02</b>	<b>27.71<math>\pm</math>2.48</b>	<b>0.97<math>\pm</math>0.02</b>	<b>27.0<math>\pm</math>2.69</b>	<b>0.93<math>\pm</math>0.03</b>
$T_1 + T_2 + T_2^* + \text{DIR} + \text{FLAIR} + \text{DWI} \dagger$	34.45 $\pm$ 4.87	<b>0.98<math>\pm</math>0.02</b>	26.8 $\pm$ 2.54	0.96 $\pm$ 0.02	25.99 $\pm$ 2.69	0.92 $\pm$ 0.03

**Direct pixel optimization** We optimized probability values directly and got the PSNRs and SSIMs for CSF, GM, and WM, respectively (See appendix Table 4). The direct pixel optimization outperforms all the other methods. One of those methods includes optimizing either 1 coefficient (*scalar optimization*) or 19 coefficients (*linear coefficients*) per pixel. The PSNR and SSIM values for coefficient optimization failed to surpass those of the baseline configuration and are off by a margin of 5.09 and 0.02 points, respectively, on average for all the maps. Additionally, examination of the results depicted in Fig 2 revealed a checkerboard pattern present in the optimized probability maps generated using this technique. Also, we tried optimizing a scalar coefficient per probability map, with all the contrasts of six sequences, which performed poorly compared to all the methods by being 14.39 and 0.47 points lower on average, respectively. Refer to the Appendix to see the detailed comparison.

Table 2: PSNR and SSIM comparisons on tissue probability maps while computing loss in Image-space and K-space domain.  $\dagger$  represents the baseline configuration.

Maps	CSF		GM		WM	
	PSNR $\uparrow$	SSIM $\uparrow$	PSNR $\uparrow$	SSIM $\uparrow$	PSNR $\uparrow$	SSIM $\uparrow$
Image-space $\dagger$	<b>34.45<math>\pm</math>4.87</b>	<b>0.98<math>\pm</math>0.02</b>	<b>26.8<math>\pm</math>2.54</b>	<b>0.96<math>\pm</math>0.02</b>	<b>25.99<math>\pm</math>2.69</b>	<b>0.92<math>\pm</math>0.03</b>
K-space	23.16 $\pm$ 8.15	0.71 $\pm$ 0.27	18.21 $\pm$ 5.02	0.75 $\pm$ 0.21	18.11 $\pm$ 4.4	0.72 $\pm$ 0.17

Table 3: PSNR and SSIM comparisons on optimizing either all maps concurrently or only a single probability map given the other two fixed.  $\dagger$  represents the baseline configuration.

Maps	CSF		GM		WM	
	PSNR $\uparrow$	SSIM $\uparrow$	PSNR $\uparrow$	SSIM $\uparrow$	PSNR $\uparrow$	SSIM $\uparrow$
All 3 $\dagger$	34.45 $\pm$ 4.87	0.98 $\pm$ 0.02	26.8 $\pm$ 2.54	0.96 $\pm$ 0.02	25.99 $\pm$ 2.69	0.92 $\pm$ 0.03
CSF	<b>40.34<math>\pm</math>10.73</b>	<b>0.99<math>\pm</math>0.01</b>	-	-	-	-
GM	-	-	<b>47.23<math>\pm</math>10.43</b>	<b>0.99<math>\pm</math>0.01</b>	-	-
WM	-	-	-	-	<b>43.33<math>\pm</math>10.65</b>	<b>0.99<math>\pm</math>0.01</b>

**All 3 maps vs. single map** From Table 3, the PSNR and SSIM metrics of single map optimization,  $(40.34 \pm 10.73, 0.99 \pm 0.02)$ ,  $(47.23 \pm 10.43, 0.99 \pm 0.01)$ , and  $(43.33 \pm 10.65, 0.99 \pm 0.01)$  for CSF, GM, and WM have always outperformed the corresponding values of optimizing all three maps concurrently. The reason why these numbers are better is because the two other known maps are fixed, which acts as a strong prior for estimating the third map. More visual results can be found in the Figure 4 of Appendix.

**Image-space vs. K-space loss** From Table 2, the PSNR and SSIM values of inferred probability maps while computing the loss in K-space domain are  $(23.16 \pm 8.15, 0.71 \pm 0.27)$ ,  $(18.21 \pm 5.02, 0.75 \pm 0.21)$ , and  $(18.11 \pm 4.4, 0.72 \pm 0.17)$  for CSF, GM, and WM respectively. These values, on average, are off by a huge margin of 9.25 and 0.23 points for PSNR and SSIM, respectively, from the baseline configuration metrics of the experiment done in Image-space, which is surprising to us. Therefore, we plan to explore more on this in our future work.

## 5 Conclusion

We have developed BMapOpt, the first framework that optimizes digital brain phantoms using an MRI differentiable simulator. Our experiments with multiple sequences demonstrate that it is possible to overcome the ill-posedness of the optimization problem. We plan to extend our work on estimating the digital brain phantoms by running our framework on large brain MRI datasets. Another direction we plan to pursue is to optimize the MRI clinical sequence parameters towards a downstream goal, such as better image contrast, better segmentation of structures, or better disease detection.

## References

1. Relaxation times for brain tissues. <https://mri-q.com/why-is-t1--t2.html>
2. Aubert-Broche, B., Evans, A.C., Collins, L.: A new improved version of the realistic digital brain phantom. *NeuroImage* **32**(1), 138–145 (2006)
3. Baum, K.G., Menezes, G., Helguera, M.: Simulation of high-resolution magnetic resonance images on the ibm blue gene/l supercomputer using simri. *Journal of Biomedical Imaging* **2011**, 1–8 (2011)
4. Benoit-Cattin, H., Collewet, G., Belaroussi, B., Saint-Jalmes, H., Odet, C.: The simri project: a versatile and interactive mri simulator. *Journal of Magnetic Resonance* **173**(1), 97–115 (2005)
5. Bittoun, J., Taquin, J., Sauzade, M.: A computer algorithm for the simulation of any nuclear magnetic resonance (nmr) imaging method. *Magnetic Resonance Imaging* **2**(2), 113–120 (1984)
6. Blystad, I., Warntjes, J.M., Smedby, Ö., Lundberg, P., Larsson, E.M., Tisell, A.: Quantitative mri for analysis of peritumoral edema in malignant gliomas. *PLoS One* **12**(5), e0177135 (2017)
7. Cao, Z., Oh, S., Sica, C.T., McGarrity, J.M., Horan, T., Luo, W., Collins, C.M.: Bloch-based mri system simulator considering realistic electromagnetic fields for calculation of signal, noise, and specific absorption rate. *Magnetic resonance in medicine* **72**(1), 237–247 (2014)
8. Cocosco, C.A.: Brainweb: Online interface to a 3d mri simulated brain database. (No Title) (1997)
9. Endres, J., Weinmüller, S., Dang, H.N., Zaiss, M.: Phase distribution graphs for fast, differentiable, and spatially encoded bloch simulations of arbitrary mri sequences. *Magnetic Resonance in Medicine* (2023). <https://doi.org/10.1002/mrm.30055>
10. Granziera, C., Wuerfel, J., Barkhof, F., Calabrese, M., De Stefano, N., Enzinger, C., Evangelou, N., Filippi, M., Geurts, J.J., Reich, D.S., et al.: Quantitative magnetic resonance imaging towards clinical application in multiple sclerosis. *Brain* **144**(5), 1296–1311 (2021)
11. Haase, A., Frahm, J., Matthei, D., Hanicke, W., Merboldt, K.D.: Flash imaging. rapid nmr imaging using low flip-angle pulses. *Journal of Magnetic Resonance* (1969) **67**(2), 258–266 (1986)
12. Hennig, J., Nauerth, A., Friedburg, H.: Rare imaging: a fast imaging method for clinical mr. *Magnetic resonance in medicine* **3**(6), 823–833 (1986)
13. Jochimsen, T.H., Schäfer, A., Bammer, R., Moseley, M.E.: Efficient simulation of magnetic resonance imaging with bloch–torrey equations using intra-voxel magnetization gradients. *Journal of Magnetic Resonance* **180**(1), 29–38 (2006)
14. Jung, B.A., Weigel, M.: Spin echo magnetic resonance imaging. *Journal of Magnetic Resonance Imaging* **37**(4), 805–817 (2013)
15. Kwan, R.S., Evans, A.C., Pike, G.B.: Mri simulation-based evaluation of image-processing and classification methods. *IEEE transactions on medical imaging* **18**(11), 1085–1097 (1999)
16. Leandrou, S., Petroudi, S., Kyriacou, P.A., Reyes-Aldasoro, C.C., Pattichis, C.S.: Quantitative mri brain studies in mild cognitive impairment and alzheimer’s disease: a methodological review. *IEEE reviews in biomedical engineering* **11**, 97–111 (2018)
17. Loktyushin, A., Herz, K., Dang, N., Glang, F., Deshmane, A., Weinmüller, S., Doerfler, A., Schölkopf, B., Scheffler, K., Zaiss, M.: Mrzero-automated discovery of mri sequences using supervised learning. *Magnetic Resonance in Medicine* **86**(2), 709–724 (2021)
18. Markl, M., Leupold, J.: Gradient echo imaging. *Journal of Magnetic Resonance Imaging* **35**(6), 1274–1289 (2012)
19. Shkarin, P., Spencer, R.G.: Direct simulation of spin echoes by summation of isochromats. *Concepts in Magnetic Resonance* **8**(4), 253–268 (1996)

20. Shkarin, P., Spencer, R.G.: Time domain simulation of fourier imaging by summation of isochromats. *International journal of imaging systems and technology* **8**(5), 419–426 (1997)
21. Stöcker, T., Vahedipour, K., Pflugfelder, D., Shah, N.J.: High-performance computing mri simulations. *Magnetic resonance in medicine* **64**(1), 186–193 (2010)
22. Summers, R.M., Axel, L., Israel, S.: A computer simulation of nuclear magnetic resonance imaging. *Magnetic resonance in medicine* **3**(3), 363–376 (1986)
23. Weigel, M.: Extended phase graphs: dephasing, rf pulses, and echoes-pure and simple. *Journal of Magnetic Resonance Imaging* **41**(2), 266–295 (2015)
24. Xanthis, C.G., Venetis, I.E., Aletras, A.H.: High performance mri simulations of motion on multi-gpu systems. *Journal of Cardiovascular Magnetic Resonance* **16**(1), 1–15 (2014)
25. Xanthis, C.G., Venetis, I.E., Chalkias, A., Aletras, A.H.: Mrisimul: a gpu-based parallel approach to mri simulations. *IEEE Transactions on Medical Imaging* **33**(3), 607–617 (2013)
26. Yoder, D.A., Zhao, Y., Paschal, C.B., Fitzpatrick, J.M.: Mri simulator with object-specific field map calculations. *Magnetic resonance imaging* **22**(3), 315–328 (2004)

## Appendix

Table 4: PSNR and SSIM comparisons of different types of optimization procedures.  $\dagger$  represents the baseline configuration.

Method	CSF		GM		WM	
	PSNR $\uparrow$	SSIM $\uparrow$	PSNR $\uparrow$	SSIM $\uparrow$	PSNR $\uparrow$	SSIM $\uparrow$
Direct pixel estimation $\dagger$	<b>34.45<math>\pm</math>4.87</b>	<b>0.98<math>\pm</math>0.02</b>	<b>26.8<math>\pm</math>2.54</b>	<b>0.96<math>\pm</math>0.02</b>	<b>25.99<math>\pm</math>2.69</b>	<b>0.92<math>\pm</math>0.03</b>
Linear coefficients	28.26 $\pm$ 4.26	0.96 $\pm$ 0.03	22.55 $\pm$ 3.06	0.94 $\pm$ 0.04	21.19 $\pm$ 2.94	0.9 $\pm$ 0.05
Scalar coefficient	16.46 $\pm$ 1.1	0.42 $\pm$ 0.09	13.69 $\pm$ 1.01	0.51 $\pm$ 0.1	13.92 $\pm$ 1.09	0.53 $\pm$ 0.07

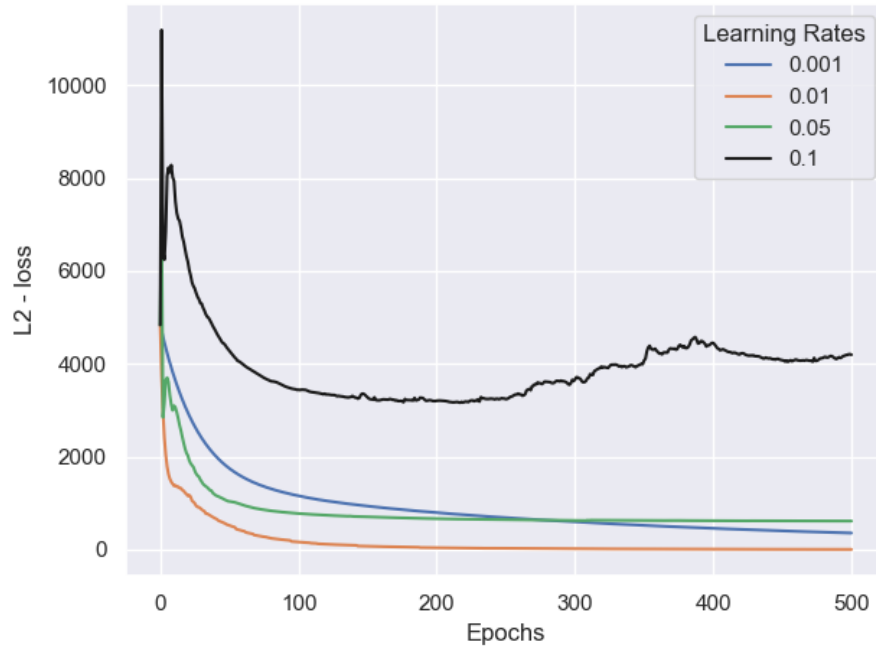


Fig. 3: Loss function for different learning rates

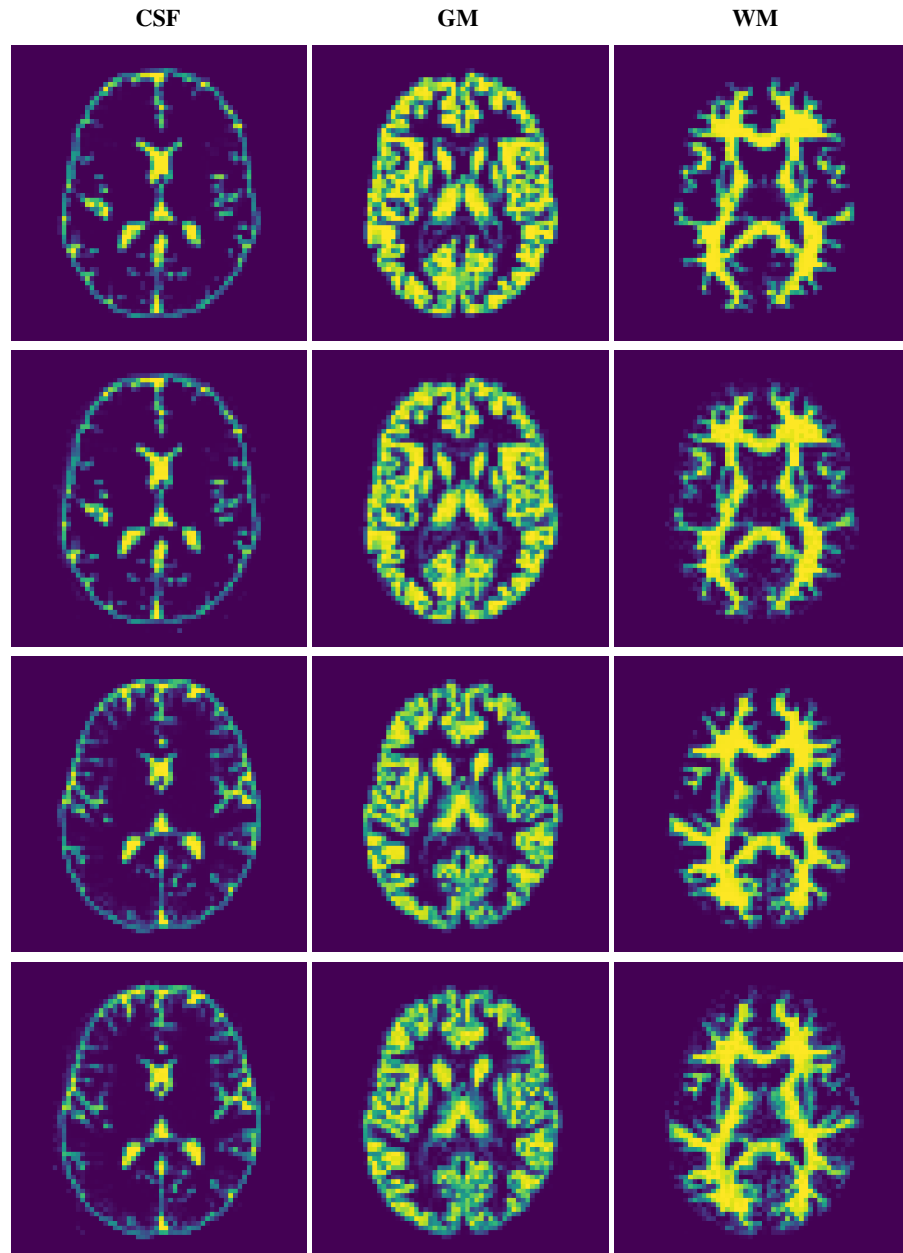


Fig. 4: From the left are CSF, GM, and WM. The first and third rows show the raw tissue probability maps for subjects 18 and 05, respectively, of the BrainWeb dataset. The second and fourth rows show the optimized probability maps using the baseline configuration for subjects 18 and 05, respectively.